ACS APPLIED ENERGY MATERIALS

www.acsaem.org Article

Elucidating and Mitigating High-Voltage Interfacial Chemomechanical Degradation of Nickel-Rich Lithium-Ion Battery Cathodes via Conformal Graphene Coating

Norman S. Luu, Jin-Myoung Lim, Carlos G. Torres-Castanedo, Kyu-Young Park, Elahe Moazzen, Kun He, Patricia E. Meza, Wenyun Li, Julia R. Downing, Xiaobing Hu, Vinayak P. Dravid, Scott A. Barnett, Michael J. Bedzyk, and Mark C. Hersam*

Cite This: *ACS Appl. Energy Mater.* 2021, 4, 11069–11079 Read Online

ACCESS | Metrics & More | Article Recommendations | Supporting Information

ABSTRACT: Lithium nickel manganese cobalt oxides (NMCs) are promising cathode materials for high-performance lithium-ion batteries. Although these materials are commonly cycled within mild voltage windows (up to 4.3 V vs Li/Li^+), operation at high voltages (>4.7 V vs Li/Li^+) to access additional capacity is generally avoided due to severe interfacial and chemomechanical degradation. At these high potentials, NMC degradation is caused by exacerbated electrolyte decomposition reactions and non-uniform buildup of chemomechanical strains that result in particle fracture. By applying a conformal graphene coating on the surface of NMC primary particles, we find significant enhancements in the high-voltage cycle life and Coulombic efficiency upon electrochemical cycling. Postmortem X-ray diffraction, X-ray photoelectron spectroscopy, and electron microscopy suggest that the graphene coating mitigates electrolyte decomposition reactions and reduces particle fracture and electrochemical creep. We propose a relationship between the spatial uniformity of lithium flux and particle-level mechanical degradation and show that a conformal graphene coating is well-suited to address these issues. Overall, these results delineate a pathway for rationally mitigating high-voltage chemomechanical degradation of nickel-rich cathodes that can be applied to existing and emerging classes of battery materials.

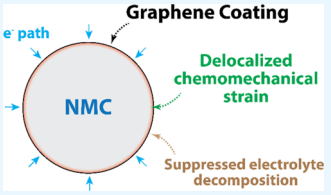

KEYWORDS: *battery cathode, lithium nickel manganese cobalt oxide, electrochemical creep, cycle life, high voltage, chemomechanical degradation, Coulombic efficiency*

1. INTRODUCTION

Lithium-ion batteries (LIBs) have emerged as the preeminent energy storage devices for renewable energy technologies. High-performance applications, including electric vehicles, often utilize cathode chemistries based on nickel-rich layered lithium nickel manganese cobalt oxides such as NMC532 ($LiNi_{0.5}Mn_{0.3}Co_{0.2}O_2$), NMC622 ($LiNi_{0.6}Mn_{0.2}Co_{0.2}O_2$), and NMC811 ($LiNi_{0.8}Mn_{0.1}Co_{0.1}O_2$).[1] Although these nickel-rich cathode materials possess intrinsically high energy densities, they suffer from severe cyclic stability issues due to chemical, structural, and mechanical deterioration of the active material during electrochemical cycling. For these reasons, the practical operating window for layered cathodes has been empirically limited to an upper cutoff voltage of 4.3 V vs Li/Li^+.[1] Nonetheless, since additional capacity and energy density can be obtained by operating LIBs over wider electrochemical voltage windows, the ability to safely and reliably utilize nickel-rich cathode materials at higher states of charge (SOCs) is greatly desired.

LIB cathode material degradation is severely exacerbated at high operating potentials (>4.7 V vs Li/Li^+). For example, electrolyte decomposition reactions such as ethylene carbonate dehydrogenation or PF_6^- decomposition become increasingly favorable at higher voltages due to the increased reactivity of lattice oxygen.[2,3] The resulting organic and lithium fluorophosphate reaction products form a solid-electrolyte interphase (SEI), which irreversibly consumes the lithium inventory and impedes subsequent ionic transport. These compounds are known to react with other electrolyte salt components to form HF, which etches the active material and further accelerates capacity fade.[4] Structurally, charging NMC-based layered oxides to high SOCs also induces severe anisotropic volumetric changes in the NMC unit cell as the c lattice parameter collapses for $x(Li) < 0.5$.[5,6] Moreover, lithium extraction results in compositional heterogeneity throughout the active material particle, which is a consequence of non-uniform distributions of interfacial chemical products, surface phases, and reaction sites.[7−9] The resulting spatial gradients in lithium concentration induce internal strains, which can be relieved

Received: July 7, 2021
Accepted: September 14, 2021
Published: September 27, 2021

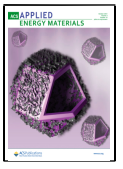

https://doi.org/10.1021/acsaem.1c01995
ACS Appl. Energy Mater. 2021, 4, 11069–11079

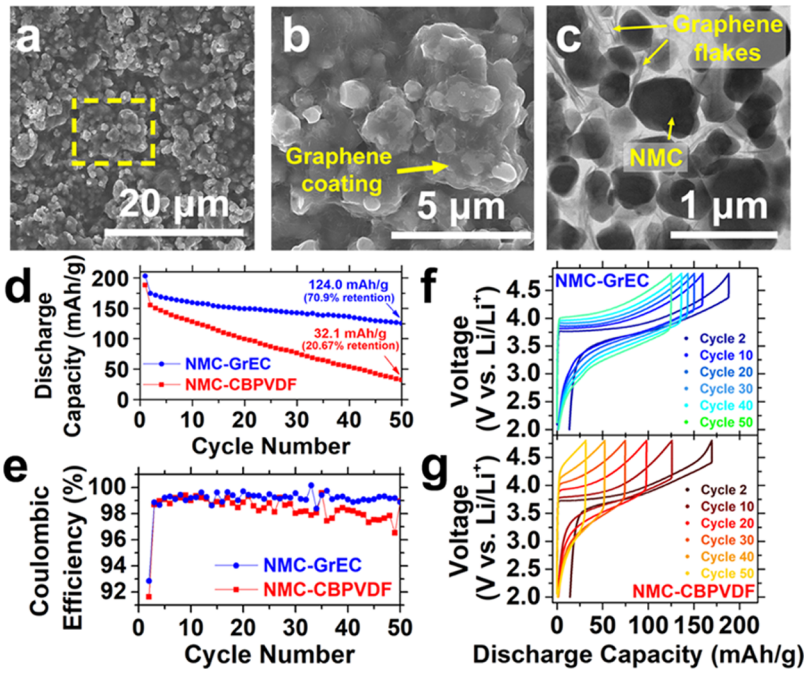

Figure 1. Morphology and electrochemical performance of graphene-coated NMC. (a) Top-down scanning electron microscopy image of the NMC-GrEC electrode. (b) Higher-magnification scanning electron microscopy image of the region outlined in yellow. (c) Bright-field transmission electron microscopy image of the NMC-GrEC electrode. (d–g) Electrochemical performance of NMC-GrEC and NMC-CBPVDF electrodes performed at 0.5C: (d) Cycle life test; (e) Coulombic efficiency; (f, g) voltage–capacity plots showing the evolution of electrode polarization for the (f) NMC-GrEC and (g) NMC-CBPVDF electrodes.

through particle cracking and intergranular fracture.[10−12] Beyond forming additional interfacial degradation sites, these cracks can also contribute to capacity fade as active material fragments become electrically isolated and electrochemically inactive.

To improve the cycle life of nickel-rich cathode materials, coating layers such as Al_2O_3,[13−15] MgO,[16] ZrO_2,[15,17] TiO_2,[18] $LiBO_2$,[19] and Li_2TiO_3[20] have been explored as interfacial buffers that scavenge HF from the electrolyte and shield the cathode surface from electrolyte decomposition reactions. However, these layers often possess low ionic and/or electronic conductivity,[21] which is detrimental to high-rate cycling. Moreover, since these coating layers are often directly bonded to the active material surface, changes in the cathode unit cell volume at high SOCs can induce mechanical delamination, irreversibly compromising the coating for future cycles.[22] Amorphous carbon coatings possessing weak carbon–carbon bonds are similarly prone to mechanical failure.[23] Therefore, a thin, conductive, conformal coating that acts as an interfacial buffer layer while accommodating mechanical changes is likely to be more effective at enabling reliable high-voltage operation of nickel-rich cathodes.

Here, we demonstrate a strategy to enhance the high-voltage cycle life and Coulombic efficiency of NMC cathodes via a conformal, conductive graphene coating. Although graphene coatings have been widely employed to improve the cycle life of Ni-rich cathode materials, most reports explore the effect of graphene coatings under mild operating voltage windows that avoid severe degradation mechanisms.[24−26] In this work, we use a high upper cutoff voltage not only to accelerate interfacial degradation, including electrolyte decomposition reactions, but also to drive chemomechanical degradation at high SOCs, such as particle fracture or electrochemical creep. Additionally, by utilizing submicron primary particles in this study, we circumvent issues of strain buildup within large secondary particle structures and ensure that exposed NMC surfaces can be uniformly coated with graphene. This strategy enables a direct investigation into the role of optimized electronic conduction pathways. Additionally, the choice to use relatively small active material particles also enables a facile morphological assessment of chemomechanical degradation since fracture and electrochemical creep events should appear on the same length scale as the particles themselves. Postmortem analysis using X-ray diffraction (XRD), X-ray photoelectron spectroscopy (XPS), and electron microscopy reveals that the graphene coating reduces the accumulation of interfacial electrolyte decomposition products and the severity of particle-level chemomechanical degradation. We propose that the graphene coating promotes spatially uniform charge transfer reactions across the electrode surface, which delocalizes cycling-induced stress and reduces the propensity for particle fracture. Moreover, the graphene coating is mechanically compliant toward unit cell volume changes at high SOCs and maintains electrical contact throughout cycling. Graphene-coated NMC cathodes therefore achieve substantially improved cycle life and Coulombic efficiencies under high-voltage operation.

2. RESULTS AND DISCUSSION

2.1. Materials Characterization. NMC532 particles were synthesized using a solid-state co-precipitation method. Synchrotron radiation powder X-ray diffraction (SR-PXRD) verified the synthesis of layered NMC532 (*R*-3*m*) with no significant evidence of impurity phases (Figure S1). Additional features in the SR-PXRD pattern, including the (006)/(102) peak splitting, confirmed the synthesis of a layered structure. Rietveld refinement indicated that the lattice parameters of the as-synthesized NMC agreed well with prior reports (Table

https://doi.org/10.1021/acsaem.1c01995
ACS Appl. Energy Mater. 2021, 4, 11069−11079

S1).[5] Inductively coupled plasma mass spectrometry (ICP-MS) was used to quantify the NMC transition metal ratio, which confirmed the target composition of 50% nickel, 30% manganese, and 20% cobalt (Table S2). Scanning electron microscopy (SEM) showed that the synthesized powder was composed of primary particles with sizes ranging from hundreds of nanometers to 1 μm in diameter (Figure S2), with no evidence of well-defined secondary particle agglomerates.

Following synthesis, the NMC particles were uniformly coated with graphene and ethyl cellulose (GrEC) using a previously established solution-phase method.[25,27] The coating conformality was confirmed using SEM and transmission electron microscopy (TEM) (Figure 1a–c), which revealed the presence of a percolating network of graphene flakes throughout the electrode, consistent with prior work.[25,27,28] After fabricating electrodes with the GrEC powder (NMC-GrEC), the electrode was heated to pyrolyze the ethyl cellulose (EC) polymer, which largely volatilizes the EC, compacts the electrode, and generates a carbon residue that helps form a percolating, electrically conductive network among the graphene-coated NMC particles.[24,25,27−30] Subsequent Raman spectroscopy of the electrode confirmed that the ratio of the D and G peaks decreased (at 1350 and 1580 cm^{-1}, respectively) (Figure S3), suggesting that EC decomposition resulted in a more graphitic carbon network that facilitates efficient charge transfer. The uncoated NMC powder was also mixed with carbon black (CB) and polyvinylidene fluoride (PVDF) to fabricate control electrodes (NMC-CBPVDF).

2.2. Electrochemical Characterization. *2.2.1. Galvanostatic Cycling.* The cycle life behavior of the NMC-GrEC and the NMC-CBPVDF electrodes was investigated using galvanostatic cycling to an upper cutoff voltage of 4.8 V vs Li/Li^+ (Figure 1d). During the activation cycle, the NMC-GrEC electrode achieved a discharge capacity of 203.1 mAh g^{-1}, whereas the NMC-CBPVDF control electrode discharge capacity reached only 188.1 mAh g^{-1}, suggesting that the graphene coating enabled increased lithium utilization from the NMC lattice. After 50 charge−discharge cycles at 0.5C, the NMC-GrEC electrode retained 70.9% of its original capacity, which was far superior to the 20.7% capacity retention observed for the NMC-CBPVDF control electrode. The extremely poor cycle life observed for the NMC-CBPVDF control electrode was attributed to two factors. First, the high primary particle surface area provided ample surfaces upon which electrolyte decomposition reactions or surface phase formation could occur.[2,3,31,32] Compared to conventional electrodes fabricated using secondary particles of NMC, the NMC-CBPVDF electrode, which utilizes submicron particles with no surface protection, exhibits a precipitous decline in cycle life. This behavior is consistent with trends for other reports utilizing comparatively larger single-crystal NMC particles.[32] Second, the high upper cutoff voltage exacerbated the severity of these interfacial chemical degradation mechanisms and promoted additional bulk chemomechanical degradation associated with layered oxides at high SOCs.[5,33] Nonetheless, the observed capacity fading reinforces the need for mitigation strategies that can enable improved high-voltage operation.

The Coulombic efficiency results (Figure 1e) also highlight the improved charge−discharge behavior of the NMC-GrEC electrodes. The first cycle Coulombic efficiency (FCE) was higher for the NMC-GrEC electrode (94.49%) than for the NMC-CBPVDF electrode (92.9%), which implies that the NMC-GrEC electrode lost fewer lithium ions to parasitic side reactions as the solid-electrolyte interphase (SEI) formed during the first cycle. This FCE is the highest reported among the many coating and doping strategies that have been attempted for NMC532 half cells at voltages beyond 4.6 V vs Li/Li^+ (Table S3). With additional cycling, the Coulombic efficiency of the NMC-GrEC electrode remained consistent after 50 cycles, while the Coulombic efficiency of the NMC-CBPVDF electrode declined after the 30th cycle. As a result, the average Coulombic efficiency of the NMC-GrEC electrode (99.68%) remained considerably higher than the average Coulombic efficiency of the NMC-CBPVDF electrode (98.57%).

The voltage−capacity plots indicate that the charge−discharge behavior was relatively stable for the NMC-GrEC electrode (Figure 1f), with only a mild polarization increase over 50 cycles. This polarization growth was again attributed to the high primary particle surface area and high cutoff voltage. On the other hand, the sudden increase in the position of the voltage shoulder (initially at ∼3.7 V vs Li/Li^+) and the increasing magnitude of the Ohmic drop between charge and discharge indicate that the inferior cycle life for the NMC-CBPVDF electrode was related to a significant increase in electrode polarization (Figure 1g). These results suggest that as the NMC-CBPVDF electrode was charged, fewer lithium ions than expected were extracted before the cutoff voltage was reached, limiting the overall per-cycle reversible capacity.

2.2.2. Electrochemical Impedance Spectroscopy. To investigate the observed improvements in the high-voltage cycling and charge−discharge behavior for graphene-coated NMC, electrochemical impedance spectroscopy (EIS) and corresponding equivalent circuit modeling were utilized to quantify changes in cell impedance. Distribution of relaxation times (DRT) analysis was also performed to accurately determine the polarization processes and the corresponding frequencies in the EIS response. The Nyquist plots for the NMC-CBPVDF and NMC-GrEC cells before cycling both show one semicircle followed by the diffusion region (Figures 2a and Figure S4). Using the corresponding DRT data (Figure S5), the semicircle was deconvoluted with three processes

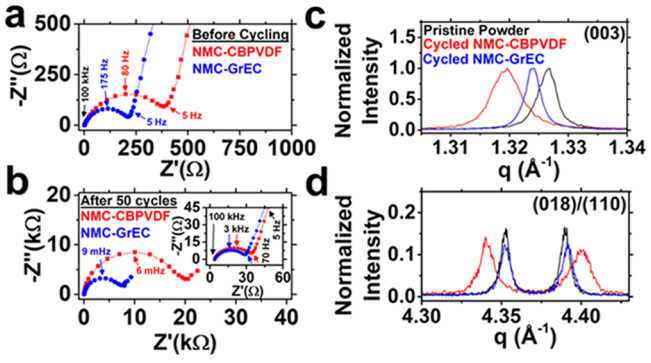

Figure 2. Additional confirmation of material degradation after cycling. (a, b) Nyquist plots obtained via electrochemical impedance spectroscopy (a) before cycling and (b) after 50 cycles. Panel (a) and the inset of (b) show zoomed-in views of the high-frequency responses. (c, d) High-resolution powder X-ray diffraction patterns near the vicinities of the (c) (003) peak and (d) (018)/(110) peaks for the pristine NMC powder and for samples that were cycled 50 times.

https://doi.org/10.1021/acsaem.1c01995
ACS Appl. Energy Mater. 2021, 4, 11069−11079

occurring at high and medium frequencies, which correspond to the electrode−current collector interface (P_1 at ∼10^5 Hz), lithium metal−electrolyte interface (P_2 at ∼10^2 Hz), and electrode−electrolyte interface (P_3 at ∼5 Hz).[34] To fit the EIS spectra, an equivalent circuit model was used that contained an inductor (L), ohmic resistance (R_0), two RQ elements that modeled P_1 and P_2, and a Randles circuit (Figure S6a) that modeled P_3 and Li-ion solid-state diffusion.

According to the results in Table S4, the NMC-GrEC electrode possesses lower charge transfer impedance (R_3 of 85 Ω) than the NMC-CBPVDF electrode (R_3 of 118 Ω) before cycling. This result is consistent with expectations gleaned from the NMC-GrEC electrode microstructure. Since the NMC particles were conformally coated with a percolating carbon network possessing intrinsically high electronic conductivity (∼10^4 S/m),[29] electrons and holes could be immediately supplied to charge compensate near sites where lithium (de)intercalation occurs. This mechanism enabled efficient charge transfer across the surfaces of the active material particles.[24,28] In contrast, carbon black particles, which possess lower intrinsic conductivities,[35] acted as point contacts between active material particles, thereby permitting only localized charge transfer.

After 50 cycles, the Nyquist plots for both electrodes each contain two semicircles and a diffusion line (Figure 2b). The DRT analysis for the samples after 50 cycles suggests that the first semicircle in the Nyquist plot (Figure 2b inset) was composed of impedances associated with the electrode−current collector (P_1) and lithium metal−electrolyte (P_2) interfaces. The process assigned to charge transfer at the electrode−electrolyte interface (P_3), which occurs at medium frequencies, increases in magnitude and shifts to lower frequencies with cycling (Figures S5 and S7b,d). The DRT analysis implies that the P_3 process comprises only a small portion of the large semicircle in the Nyquist plot of the cells after 50 cycles (Figure 2b). The remainder of the second semicircle corresponds to a fourth process at lower frequencies (P_4 at ∼9 mHz) and was assigned to degradation processes at high voltage. Importantly, this conclusion was corroborated by additional DRT tests performed on replicate NMC-CBPVDF and NMC-GrEC electrodes cycled between 2.0 and 4.3 V vs Li/Li^+ at the same applied current rate (see analysis in the Supplementary Information and Figures S7a,c and S8a,b). The DRT response of these replicate cells shows a P_4 process with a negligible magnitude when compared to the DRT response of the cells cycled at high voltage, providing strong evidence for a relationship between the cutoff voltage and the magnitude of the P_4 polarization (Figure S7). The voltage-dependent activation of this process suggests that it could be related to degradation mechanisms at high voltages, such as chemo-mechanical changes in the active material or the formation of a thick chemical interphase. Correspondingly, another RQ element was added to the equivalent circuit model and used to fit the high-voltage EIS data after cycling (Figure S6b).

According to the fit results (Table S4), the charge transfer impedance (R_3) for both electrodes increased after 50 cycles. This increase was greater for the NMC-CBPVDF electrode (180 Ω, corresponding to a 153% increase) compared to the NMC-GrEC electrode (120 Ω, corresponding to a 141% increase). Moreover, the magnitude of the surface film impedance (P_4) at low frequencies was significantly higher in the NMC-CBPVDF (18,500 Ω) electrode compared to the NMC-GrEC electrode (6850 Ω). These EIS results, coupled with the galvanostatic cycling data, suggest that active material degradation accumulated in a manner that increased the electrode charge transfer impedance. However, since these impedance values were lower for the NMC-GrEC electrode, the graphene coating apparently mitigated NMC degradation and ensured a more efficient charge−discharge process. Finally, the improved electrochemical performance of the NMC-GrEC electrode was likely related to the significantly lower R_4 impedance associated with high-voltage degradation.

2.3. Postmortem Characterization. *2.3.1. High-Resolution X-ray Diffraction.* To further explain the electrochemical results, high-resolution SR-PXRD was performed on fully discharged samples to investigate cycling-induced structural changes. Since the NMC unit cell dimensions are highly dependent on the SOC, discharging the electrodes to the same voltage and then measuring the (110) and the (003) peak positions can elucidate differences between the lithium content of the two samples. As NMC is charged to moderate SOCs, lithium is removed from the NMC structure, causing the unit cell to contract in the $a = b$ directions and expand in the c direction since unoccupied sites in the lithium layer promote oxygen−oxygen repulsion across the resulting van der Waals gap. During charging, the NMC (110) peak is known to shift to higher angles, while the (003) peak shifts to lower angles.[5,6] Although these peaks are expected to return to their original positions at the end of discharge, the postmortem diffraction patterns showed that this phenomenon was not the case for the (110) and the (003) peaks in the cycled samples (Figure 2c,d). The deviations in the diffraction peak positions are more severe for the NMC-CBPVDF electrode, suggesting that a large population of NMC was unable to relithiate during the 50th cycle discharge step. This result could occur for multiple reasons, including the formation of interfacial electrolyte decomposition products that kinetically limit charge transfer reactions or cycling-induced volumetric changes that cause cracking, particle fracture, or detachment from the conductive path to the current collector. Charging to higher SOCs is also known to induce mechanical degradation due to a collapse of the c axis of the unit cell.[5,36,37] Importantly, postmortem scanning transmission electron microscopy and ICP-MS analysis show that the cycling irreversibility was not due to differences in surface rocksalt phase formation or transition-metal dissolution between the two samples (see Figure S9, Table S5, and corresponding STEM and ICP-MS analyses in the Supporting Information). Nonetheless, the SR-PXRD results corroborate the galvanostatic cycling and EIS results, further suggesting that the graphene-coated electrode experienced reduced material degradation compared to the control sample.

2.3.2. X-ray Photoelectron Spectroscopy. XPS was then used to investigate the differences between the surface chemistries of the two electrodes before and after cycling. The C 1s spectra for both electrodes before cycling show an intense peak at 284.8 eV, corresponding to C−C bonds (Figure 3) from adventitious carbon and the conductive carbon additives. The NMC-CBPVDF electrode also exhibits spectral intensities in the range of reported values for C−O bonds (286.1 eV) and C═O/O−C−O bonds (287.4 eV), which likely originate from carbon−oxygen surface functional groups on carbon black.[38] In contrast, the C 1s spectrum for the pristine NMC-GrEC electrode surface is dominated by the C−C bonding character, consistent with previous reports for pyrolyzed graphene-ethyl cellulose films.[25,29,39,40] The differ-

https://doi.org/10.1021/acsaem.1c01995
ACS Appl. Energy Mater. 2021, 4, 11069−11079

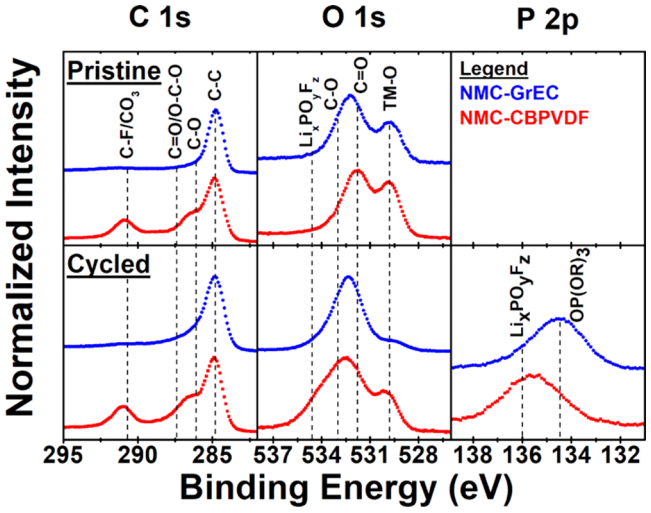

Figure 3. XPS C 1s, O 1s, and P 2p spectra of the NMC-GrEC and NMC-CBPVDF electrodes before cycling (top) and after cycling (bottom). The P 2p spectra for the pristine samples were not taken since the phosphorus character will only be present after electrolyte contact.

ence in the C−F bond intensities near 290.7 eV is attributed to the absence of polyvinylidene fluoride binder in the NMC-GrEC electrode.

Following electrochemical cycling, the C 1s and O 1s XPS spectra exhibit increased spectral intensities at binding energies corresponding to carbon−oxygen bonds in both electrodes, likely due to the formation of interfacial organic decomposition products (Figure 3). This conclusion is supported by the growth of carbon−oxygen bond intensities (C═O at 531.8 eV and C−O at 533.2 eV) and the decrease in transition metal-oxygen bond intensities (529.1 eV) in the O 1s spectra. Similarly, the Mn 3p and the Co 3p peaks are initially prominent in the Li 1s XPS spectra for both pristine samples but significantly decrease in intensity after cycling (Figure S10). These trends suggest that an organic-rich SEI layer formed during cycling that attenuated the transition metal-oxygen signal from the NMC bulk (Figure 3), consistent with the galvanostatic cycling and the EIS results. While carbon black is known to react with electrolyte components to form organic decomposition products,[41] the absence of out-of-plane dangling bonds on graphene likely minimizes its chemical reactivity with the electrolyte. Indeed, the C 1s spectrum for the NMC-GrEC electrode after cycling is still dominated by C−C spectral intensities, suggesting that the graphene coating successfully maintains a highly conductive surface over the operating lifetime of the cell.

The chemical natures of the inorganic degradation products differ between the two cycled electrodes (Figure 3). The Li 1s and the F 1s spectra (Figure S10) suggest that LiF (56.1 eV and 685.4 eV), a $LiPF_6$ salt decomposition product,[42] is present in both cycled samples. Additional salt degradation reactions generate phosphate compounds, which can subsequently react with lattice lithium to form $Li_xPO_yF_z$ species.[3] Significantly, the P 2p spectrum (Figure 3) for the cycled NMC-CBPVDF electrode shows prominent spectral intensities at binding energies close to reported values for $Li_xPO_yF_z$ (136.0 eV), whereas the NMC-GrEC electrode exhibits greater intensities close to the binding energies reported for phosphates (134.5 eV). These results imply that fewer fluorophosphate degradation products were present on the NMC-GrEC electrode. Since the graphene coating presumably limits the amount of electrolyte that can contact the active material surface, it reduces interactions between charged oxide surfaces and electrolyte solvent molecules, kinetically suppressing dissociation reactions such as ethylene carbonate dehydrogenation.[2,3] Moreover, the coating also limits the contact between the electrode surface and phosphate-based reaction intermediates, which can generate surface protic species that form HF and $Li_xPO_yF_z$. Together, these benefits likely result in preserved lithium inventory, reduced active material etching, and ultimately improved Coulombic efficiency and cycle life.

2.3.3. Scanning Electron Microscopy. Finally, postmortem SEM was performed on the cycled electrodes to investigate morphological changes that occurred during cycling. First, interparticle cracking was observed (Figure 4), which likely

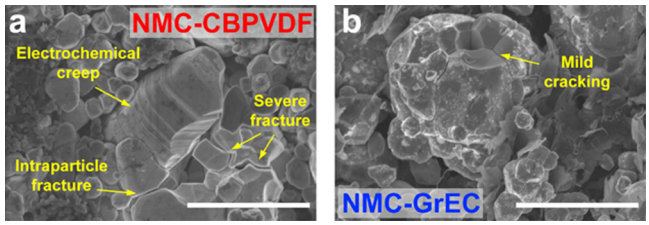

Figure 4. Postmortem scanning electron microscopy images of the (a) NMC-CBPVDF electrode surface and (b) NMC-GrEC electrode surface. Both scale bars are 2 μm.

originated from anisotropic changes in the unit cell volume at high SOCs or spatially non-uniform charge transfer reactions between particles, both of which would generate strain energy that drive particle fracture. Second, intraparticle cracking was observed in primary particles. The NMC-CBPVDF electrode showed significant signs of both failure modes, with wide gaps forming between individual primary particles (Figures 4a and Figure S11). In contrast, fewer and thinner intraparticle and interparticle cracks were found on particles in the NMC-GrEC electrode (Figures 4b and Figure S12). Third, electrochemical creep was observed, as evidenced by a terrace-like surface morphology on primary particles. This phenomenon is consistent with lattice-invariant shear associated with the O3 to O1 phase transformation for layered cathode materials[33] such as $LiCoO_2$,[43−46] $LiNiO_2$,[47−49] and NMC.[36,50] Significantly, the severity of electrochemical creep was much lower in the NMC-GrEC electrode (Figures 4b and Figure S12). To confirm that this observation was consistent across different areas on the electrodes, over 2000 primary particles on each electrode were analyzed via SEM to identify signs of electrochemical creep. Approximately 18% of the primary particles evaluated for the NMC-CBPVDF electrode showed terracing, compared to only 6% of the primary particles evaluated for the NMC-GrEC electrode.

Furthermore, evidence of changes in the particle morphology was correlated to differences between the SR-PXRD patterns of the pristine and cycled samples. The magnitude of the changes in the (110) and the (003) full-width half maxima (Figure 2c,d) after cycling suggested that the domain sizes and microstrain amounts evolved differently between the two samples, which was consistent with the mechanical deformation observed in SEM. Rietveld refinement of the SR-PXRD patterns for the cycled samples revealed that the domain size

https://doi.org/10.1021/acsaem.1c01995
ACS Appl. Energy Mater. 2021, 4, 11069−11079

decreased and the microstrain increased for the NMC-CBPVDF sample after cycling. In contrast, no significant changes were found between the NMC-GrEC sample and the pristine NMC powder (Figure S13 and Table S1). Therefore, postmortem SEM provided a morphological confirmation of chemomechanical degradation after cycling to high SOCs, corroborating the SR-PXRD and Rietveld refinement results.

2.3.4. Discussion. The observed electrochemical performance enhancement in the NMC-GrEC electrodes is likely related to the improved lithiation dynamics enabled by a conformal carbon coating. Prior work has identified compositional heterogeneity across active material particle surfaces during cycling.[7−9,51] In secondary particle-based electrodes, reaction non-uniformity is related to the contact between adjacent primary particles, which can change as a result of cycling-induced anisotropic strains, as well as the electrolyte penetration into the interior of the agglomerate.[8,12,52,53] In these structures, intergranular fracture is a well-known failure mechanism that underlies capacity fading due to the loss of electrical contact between individual grains. Therefore, using primary particles in this work ensures that all NMC surfaces that could be exposed to the electrolyte during cycling were coated by a conductive carbon layer, thus enabling an investigation into the relationship between surface electronic conductivity and charge-transfer-induced chemomechanical degradation. For primary particles, other factors can also contribute to reaction non-uniformity, such as crystallographically anisotropic lithium diffusivities or the presence of high-impedance surface phases.[8] The graphene coating demonstrated in this work is unlikely to affect these sources of compositional heterogeneity since they are inherent to the material system. However, a surface coating nonetheless presents an opportunity to engineer the dynamics of interfacial charge transfer reactions in the context of electronic connectivity within the electrode, which is highly important irrespective of the particle size or composition.[8]

Since intercalation reactions depend on electrically conductive pathways for charge compensation, a conductive network based on non-uniformly distributed carbon black particles results in high spatial variations in surface electrical resistance,[54] promoting hotspots with high lithium-ion current densities on the particle surface. During charging, regions neighboring these current hotspots would be delithiated first, with two implications for mechanical degradation. First, lithium-poor and lithium-rich regions with different molar volumes would exist simultaneously within a particle, generating a corresponding stress field that varies with lithium content. Non-uniform stress and strain distributions are likely precursors to intraparticle and interparticle fracture.[37,55,56] Second, highly delithiated regions can act as nucleation sites for the high-voltage O3 to O1 phase transition that induces electrochemical creep.[33] In contrast, a layer that can supply or accept electrons anywhere on the particle surface, such as a graphene coating, delocalizes these hotspots and thereby promotes more spatially uniform compositional and volumetric changes during cycling (Scheme 1). We anticipate that future studies will continue to explore the relationship between surface conduction and reaction uniformity, utilizing techniques such as scanning transmission X-ray microscopy that allow visualization of the SOC within a single particle via Ni K-edge mapping. It is also important to consider the possibility that delithiation induces changes in the NMC electrical conductivity, which could generate new electrical conduction pathways at high SOCs. However, since the electrical conductivity of GrEC films is 3 orders of magnitude greater than that of layered lithium transition metal oxides (10^4 S/m vs 10^1 S/m),[29,57,58] electrons are likely to continue to conduct along the graphene network even if the NMC bulk electrical conductivity changes.

Scheme 1. Schematic Showing Proposed Degradation Mechanisms for the (a) NMC-CBPVDF Electrode, Which Are Mitigated in the (b) NMC-GrEC Electrode Due to the Presence of the Graphene Coating

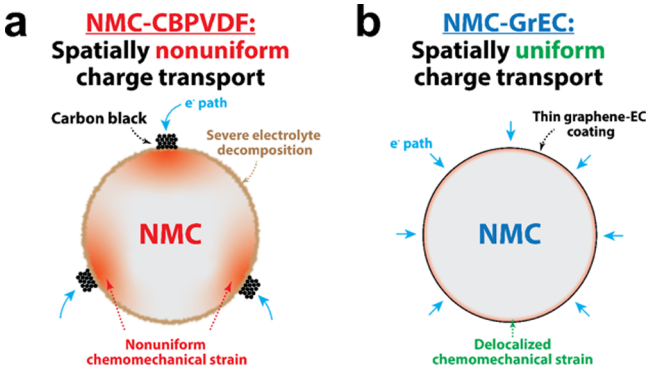

A feedback loop exists between particle-level mechanical degradation and changes in interfacial chemistry, crystallography, and electrochemical activity. Cracking and lattice-invariant shear both generate new surfaces that quickly react with the electrolyte, which can lead to additional SEI or rocksalt phase formation. Effective mitigation of particle-level mechanical degradation can address these issues, therefore enabling lower electrode polarization and improved Coulombic efficiency during long-term cycling. In addition, although fracture-initiated particle detachment can significantly contribute to capacity fade,[54] this negative effect can be reduced by engineering the electronic conduction path within an electrode. Here, the conformal graphene network plays this role since it acts as a conductive network that captures particle fragments generated via intraparticle and interparticle fracture, thereby ensuring that fragments remain electrochemically active. This mechanism has been proposed to explain cycle life improvements in other systems that undergo volume expansion during lithiation, such as graphene-coated silicon microparticles.[23]

Finally, the conductive graphene coating possesses electrode engineering advantages over other inorganic coating layers that have been employed to stabilize the electrode−electrolyte interface.[21,22] To overcome the low electrical conductivity of these materials, one approach is to increase the fraction of conductive carbon in the electrode. However, this strategy results in compromised electrode-level energy densities. In contrast, electrodes utilizing graphene-coated NMC have intrinsically higher packing densities than electrodes fabricated with an equivalent fraction of carbon black (Figure S14a,b), resulting in high volumetric capacities even at high applied current rates (Figure S14c). These positive impacts across multiple length scales are enabled by the intrinsically robust mechanical, chemical, and electronic properties of graphene that present distinct advantages over other surface coating schemes.

https://doi.org/10.1021/acsaem.1c01995
ACS Appl. Energy Mater. 2021, 4, 11069−11079

3. CONCLUSIONS

In this work, we showed that a conformal graphene coating comprehensively enhances the high-voltage electrochemical performance of NMC cathode materials, including significantly improved cycle life, increased Coulombic efficiency, and slower impedance growth. XPS analysis revealed that graphene-coated NMC electrodes exhibited reduced spectral intensities corresponding to electrolyte decomposition products, suggesting that the interfacial graphene layer minimizes parasitic interactions between the electrode and electrolyte. Postmortem electron microscopy showed that the cycling improvements were also related to suppressed mechanical degradation, evidenced by fewer signs of cracking and electrochemical creep for the graphene-coated NMC particles. This observation was consistent with fewer changes in the crystallite size and microstrain values obtained from Rietveld refinement following high-resolution SR-PXRD. Therefore, we propose that the conformal graphene coating enables spatially uniform charge transfer reactions across the particle surface, delocalizing cycling-induced stress that can initiate mechanical degradation. Overall, this study highlights the importance of the relationships among interfacial coating layers, lithiation dynamics, and chemomechanical degradation of the active material, which is highly relevant for the development of systematic engineering strategies aimed at improving the performance of high-voltage LIB electrode materials.

4. EXPERIMENTAL METHODS

4.1. NMC Synthesis. A solid-state co-precipitation method was used to synthesize the NMC532 active material. Ni(II) acetate tetrahydrate, Mn(II) acetate tetrahydrate, and Co(II) acetate tetrahydrate precursors (MilliporeSigma) were dissolved in deionized water in a 5:3:2 molar ratio, yielding a 0.2 M transition metal precursor solution. At the same time, oxalic acid dihydrate (MilliporeSigma) was dissolved in deionized water to form a 0.1 M solution of oxalic acid. After 10 min of stirring at 300 RPM, the oxalic acid solution was added dropwise to precipitate the precursors from the solution. The mixture was then further stirred at 300 RPM for 3 h before the water was evaporated using a rotary evaporator (Buchi Rotavapor R-300 System). The resulting powder was dried overnight under dynamic vacuum at 80 °C and then subsequently calcined at 450 °C under 50 sccm of flowing oxygen for 6 h using a tube furnace (Thermo Scientific Lindberg Blue M). After the powder cooled to room temperature, lithium hydroxide monohydrate (MilliporeSigma) was added in a 3 mol % excess and uniformly mixed into the powder using a mortar and pestle. The final powder mixture was calcined under flowing oxygen at 550 °C for 8 h and then was subsequently heated to 850 °C for 12 h, ultimately yielding stoichiometric NMC532. All ramp rates used were 5 °C/min.

4.2. Graphene Exfoliation. The graphene/ethyl cellulose (graphene/EC) powder was prepared by mixing 100 g of 150 mesh flake graphite (MilliporeSigma), 6 g of ethyl cellulose powder (4 cP, MilliporeSigma), and 1 L of 200 proof ethanol (Decon Labs) using a Silverson L5M-A shear mixer for 2 h at 10,230 RPM. Large, unexfoliated graphite flakes were removed from the dispersion by centrifuging at 7500 RPM for 20 min using a Beckman Coulter J26 XPI centrifuge. Following centrifugation, the supernatant was harvested and flocculated by adding a solution of NaCl in water (0.04 g/mL) to reach a final ratio of 1.74:1 graphene dispersion:sodium chloride solution. This mixture was then centrifuged again at 7500 RPM for 7 min to sediment the graphene/ethyl cellulose powder. The powder was collected, thoroughly rinsed with deionized water to remove residual sodium chloride, vacuum-filtered, and dried under an infrared lamp overnight. Thermogravimetric analysis revealed that the resulting powder possessed a graphene fraction of approximately 33 wt %.

4.3. Electrode Fabrication. The NMC-CPBVDF electrode slurry was prepared by homogeneously mixing a 90:5:5 weight ratio of NMC, Super P (Alfa Aesar), and polyvinylidene fluoride (PVDF, MTI Corporation) with *N*-methyl-2-pyrrolidone (NMP, MilliporeSigma) using a centrifugal mixer (Thinky USA). To promote better homogeneity and viscosity in the electrode slurry, PVDF was first mixed with NMP at 80 °C overnight to form a 6 wt % solution. To fabricate the graphene electrodes (NMC-GrEC), graphene/EC powder and multiwalled carbon nanotubes (MWCNT, MilliporeSigma) were dispersed in ethanol for 1 h using a Fisher Scientific Sonic Dismembrator Model 500 set at a power output of 40 W. To match the carbon content of the control electrode (i.e., 5% conductive carbon), a 95:4.5:0.5 ratio of NMC, graphene, and MWCNT was used. Here, a small amount of MWCNT was added to improve the mechanical integrity of the binder-free electrode. Additionally, since prior work found that only 0.5 wt % graphene is needed to conformally coat $LiNi_{0.8}Co_{0.15}Al_{0.05}O_2$ secondary particles,[24] 4.5 wt % graphene was used in this work to ensure that all primary particle surfaces were coated. Any remaining graphene flakes formed a composite with the graphene-coated NMC particles that promoted charge transport within the electrode.

To promote better homogeneity and slurry stability during electrode casting, a solvent exchange with NMP was performed. NMP was added to the graphene/EC-MWCNT-ethanol dispersion, and the ethanol was subsequently removed by stirring the graphene/EC-MWCNT-NMP-ethanol solution on a hot plate set at 70 °C. Following the solvent exchange, NMC powder was annealed at 250 °C for 1 h in flowing oxygen and then mixed with the exfoliated graphene/EC-MWCNT solution using a centrifugal mixer (Thinky, USA). Both slurries were cast onto aluminum foil and dried at 120 °C in a convection oven followed by a second drying step at 80 °C under dynamic vacuum. Although the NMC-GrEC electrode contained no additional polymeric binder, the MWCNTs and the conductive carbon residue formed by the decomposition of the ethyl cellulose together acted as the binding components in the electrode. Consequently, no film delamination was observed during casting and drying, which was consistent with previous reports.[25,27] The average active material loadings for both the NMC-CBPVDF and the NMC-GrEC electrodes were maintained at ∼3 mg cm^{-2}. Electrode discs were punched out and calendered with approximately 6 MPa applied pressure. A micrometer (Mituyo) was used to measure the thickness of the electrodes. For NMC-GrEC electrodes, ethyl cellulose was removed from the electrodes via thermal annealing at 250 °C in flowing oxygen for 1 h. 2032-type two-electrode coin cells were assembled in an Ar glovebox (VAC Omni-Lab) versus a lithium (Alfa Aesar) counter electrode and 1 M $LiPF_6$ in 1:1 vol/vol ethylene carbonate/ethyl methyl carbonate (EC/EMC, MilliporeSigma) as the electrolyte. The separator used was Celgard 2325.

4.4. Electrochemical Characterization. Galvanostatic cycling was performed between 2.0 and 4.8 V vs Li/Li^+ using an Arbin LBT-20084 battery cycler. Prior to cycling at 0.5C, electrodes were activated using a 0.1C constant current-constant-voltage (CCCV) protocol. Specifically, after a galvanostatic step, cells were held at the respective cutoff voltage until the current reached C/20. Rate capability tests were performed using a constant charge-fast discharge protocol. Electrochemical impedance spectroscopy measurements were performed on fully charged electrodes using a Bio-Logic VSP potentiostat between 1 MHz and 1 mHz. Distribution of relaxation times analysis was performed using the DRTtools MATLAB toolbox.[59]

4.5. Raman Spectroscopy. Raman spectra were collected with a Horiba Scientific XploRA PLUS Raman microscope with a 532 nm laser excitation wavelength at 16.75 mW laser power and an 1800 g/mm grating for 20 s.

4.6. X-ray Diffraction. Synchrotron radiation powder X-ray diffraction (SR-PXRD) experiments were carried out on Beamline 5-BMC at the Advanced Photon Source (APS) at an energy of 19.97 keV (λ = 0.6208 Å). After cycling, NMC powder was harvested from cycled electrodes inside an Ar glovebox. The powders were then transferred into capillaries and sealed shut. During acquisition, the

https://doi.org/10.1021/acsaem.1c01995
ACS Appl. Energy Mater. 2021, 4, 11069−11079

capillaries were continuously rotated about a horizontal axis. The incoming X-ray beam spot size was 2 × 8 mm^2. The powder diffractometer was employed in a high-resolution Bragg−Brentano geometry with a double bounce pseudo-channel-cut crystal configuration of two Si(111) crystals. In the detector arm, an anti-scatter flight tube followed by Soller slits with a vertical blade was employed to limit horizontal axial divergence. To improve resolution, a Ge(220) analyzer crystal was utilized before acquiring the signal with an Oxford Cyberstar scintillation counter. Rietveld analysis was performed with GSAS-II software.[60] The refined parameters were the lattice constants (a and c), sample displacement, crystallite size and microstrain (both isotropic), and the Ni in Li site fraction. The standard reference material LaB_6 was utilized to obtain the appropriate instrument profile parameters of the setup.

4.7. Inductively Coupled Plasma Mass Spectrometry. To analyze the transition metal ratio of the synthesized NMC, a small amount of synthesized NMC powder was added directly into a 50/50 mixture of trace-grade nitric acid and hydrochloric acid. After complete digestion of the powder overnight at 65 °C, ultrapure water was added to dilute the solution to a 4% (v/v) acid concentration in a sample volume of 10 mL. To quantify transition metal dissolution in pristine samples, NMC-GrEC and NMC-CBPVDF electrodes with the same active material mass loading were each immersed in 1 mL of 1 M $LiPF_6$ in 1:1 vol/vol ethylene carbonate/ethyl methyl carbonate (EC/EMC, MilliporeSigma), sealed under argon, and placed in an oven at 60 °C. Two replicates were made for each sample. After 7 days, the electrolyte was harvested and digested overnight using trace-grade nitric acid in a water bath set at 65 °C. Following digestion, the solution was diluted to a 3% (v/v) acid concentration in a 5 mL sample volume. All ICP analysis was performed using a ThermoFisher iCAP Q ICP-MS.

4.8. X-ray Photoelectron Spectroscopy. Postmortem X-ray photoelectron spectroscopy measurements were performed using a Thermo Scientific ESCALAB 250 Xi+ system (Al Kα radiation, ~1486.6 eV) at a pressure of ~5 × 10^{-8} Torr. Acquisition was performed using a 900 μm spot size. Samples were charge compensated with a flood gun. To prepare samples for XPS analysis, coin cells were disassembled inside an Ar glovebox and thoroughly rinsed with dimethyl carbonate. After drying on a hot plate inside the glovebox at 120 °C for 48 h, the electrodes were transferred into the XPS analysis chamber using a sealed transfer vessel to prevent ambient exposure. All peaks were charge corrected to adventitious carbon at ~284.8 eV.

4.9. Scanning Electron Microscopy. Scanning electron microscopy was performed using a Hitachi SU8030 SEM. Cross-sectional samples were prepared by immersing electrode discs in liquid nitrogen for 20 s prior to cleaving with a razor blade. The electrochemical creep and fracture analysis was performed at various points across the surfaces of the NMC-CBPVDF and NMC-GrEC electrodes to ensure that representative statistics were acquired. Approximately 2000 particles were assessed for electrochemical creep and fracture in both electrode compositions. Particles were considered to be fractured if the gap distance formed by particle fracture was ~10 nm or greater. Similarly, particles were considered to have experienced electrochemical creep only if a terraced morphology was evident on the surface. Since a thick layer of graphene flakes could obfuscate the NMC surface during SEM analysis, both electrodes were slightly scratched using a razor blade to allow imaging of particles buried in the interior of the electrode. Particle surfaces on both the NMC-CBPVDF and NMC-GrEC electrodes were then analyzed in various regions on the electrode surface and subsurface.

4.10. Scanning Transmission Electron Microscopy. Electrodes were prepared for scanning transmission electron microscopy (STEM) analysis by focused ion beam (FIB) milling on a FEI Helios Nanolab SEM/FIB. STEM investigations were performed using a JEOL JEM ARM200CF aberration-corrected STEM that was operated at 200 kV.

■ ASSOCIATED CONTENT

Supporting Information

The Supporting Information is available free of charge at https://pubs.acs.org/doi/10.1021/acsaem.1c01995.

Experimental methods, comparison of first cycle efficiencies, electrochemical impedance spectroscopy (EIS) and distribution function of relaxation times (DRT) analysis, postmortem scanning transmission electron microscopy (STEM) analysis, postmortem inductively coupled plasma mass spectrometry (ICP-MS) analysis, Li 1 s and F 1 s spectra from X-ray photoelectron spectroscopy (XPS), additional postmortem scanning electron microscopy (SEM) images, postmortem synchrotron radiation powder X-ray diffraction (SR-PXRD) patterns, Rietveld refinement results, electrode cross-sectional images, volumetric capacity comparison (PDF)

■ AUTHOR INFORMATION

Corresponding Author

Mark C. Hersam − *Department of Materials Science and Engineering, Northwestern University, Evanston, Illinois 60208, United States; Applied Physics Program and Department of Chemistry and Department of Electrical and Computer Engineering, Northwestern University, Evanston, Illinois 60208, United States;* orcid.org/0000-0003-4120-1426; Email: m-hersam@northwestern.edu

Authors

Norman S. Luu − *Department of Materials Science and Engineering, Northwestern University, Evanston, Illinois 60208, United States*

Jin-Myoung Lim − *Department of Materials Science and Engineering, Northwestern University, Evanston, Illinois 60208, United States;* Present Address: Hunt Energy Enterprises, 1900 North Akard Street, Dallas, Texas 75201-2300, United States (J.-M.L.)

Carlos G. Torres-Castanedo − *Department of Materials Science and Engineering, Northwestern University, Evanston, Illinois 60208, United States*

Kyu-Young Park − *Department of Materials Science and Engineering, Northwestern University, Evanston, Illinois 60208, United States;* Present Address: Graduate Institute of Ferrous and Energy Materials Technology, Pohang University of Science and Technology, Pohang, Kyungbuk 37673, Republic of Korea (K.-Y.P.)

Elahe Moazzen − *Department of Materials Science and Engineering, Northwestern University, Evanston, Illinois 60208, United States*

Kun He − *Department of Materials Science and Engineering, Northwestern University, Evanston, Illinois 60208, United States; NUANCE Center, Northwestern University, Evanston, Illinois 60208, United States;* orcid.org/0000-0001-5504-5458

Patricia E. Meza − *Department of Materials Science and Engineering, Northwestern University, Evanston, Illinois 60208, United States*

Wenyun Li − *Department of Materials Science and Engineering, Northwestern University, Evanston, Illinois 60208, United States; NUANCE Center, Northwestern University, Evanston, Illinois 60208, United States*

Julia R. Downing − *Department of Materials Science and Engineering, Northwestern University, Evanston, Illinois 60208, United States*

Xiaobing Hu − *Department of Materials Science and Engineering, Northwestern University, Evanston, Illinois 60208, United States; NUANCE Center, Northwestern University, Evanston, Illinois 60208, United States;* orcid.org/0000-0002-9233-8118

Vinayak P. Dravid − *Department of Materials Science and Engineering, Northwestern University, Evanston, Illinois 60208, United States; NUANCE Center, Northwestern University, Evanston, Illinois 60208, United States;* orcid.org/0000-0002-6007-3063

Scott A. Barnett − *Department of Materials Science and Engineering, Northwestern University, Evanston, Illinois 60208, United States;* orcid.org/0000-0001-9813-7360

Michael J. Bedzyk − *Department of Materials Science and Engineering, Northwestern University, Evanston, Illinois 60208, United States; Department of Physics and Astronomy and Applied Physics Program, Northwestern University, Evanston, Illinois 60208, United States;* orcid.org/0000-0002-1026-4558

Complete contact information is available at: https://pubs.acs.org/10.1021/acsaem.1c01995

Notes

The authors declare the following competing financial interest(s): M.C.H. declares a financial interest in Volexion, Inc., which is a spinout company focused on high-performance LIB cathode materials.

■ ACKNOWLEDGMENTS

The authors thank Cesar Villa for helpful discussions about TEM, as well as Dr. Lei Li and Dr. Kan-Sheng Chen for early discussions on this project. This work was primarily supported by the Exelon Corporation. Graphene powder production was supported by the National Science Foundation Scalable Nanomanufacturing Program (NSF CMMI-1727846 and NSF CMMI-2039268) and the National Science Foundation Future Manufacturing Program (NSF CMMI-2037026). Electrochemical characterization was supported by the Center for Electrochemical Energy Science, an Energy Frontier Research Center funded by the U.S. Department of Energy (DOE), Office of Science, Basic Energy Sciences under Award No. DE-AC02-06CH11357. Synchrotron radiation powder X-ray diffraction was performed at the DuPont-Northwestern-Dow Collaborative Access Team (DND-CAT) located at Sector 5 of the Advanced Photon Source (APS). DND-CAT is supported by Northwestern University, The Dow Chemical Company, and DuPont de Nemours, Inc. This research used resources of the Advanced Photon Source, a U.S. Department of Energy (DOE) Office of Science User Facility operated for the DOE Office of Science by Argonne National Laboratory under Contract No. DE-AC02-06CH11357. The authors thank DND-CAT Engineer Mike Guise for his valuable assistance in the beamline during the COVID-19 pandemic. The authors also thank DND-CAT Director Denis T. Keane for his support and helpful discussions. This work made use of the Keck-II and EPIC facilities of the Northwestern University NUANCE Center, which has received support from the SHyNE Resource (NSF ECCS-1542205), the IIN, and the Northwestern University MRSEC program (NSF DMR-1720139). Metal analysis was performed at the Northwestern University Quantitative Bio-Element Imaging Center, which is supported by NASA Ames Research Center NNA06CB93G.

■ REFERENCES

(1) Li, W.; Erickson, E. M.; Manthiram, A. High-Nickel Layered Oxide Cathodes for Lithium-Based Automotive Batteries. *Nat. Energy* **2020**, *5*, 26−34.

(2) Giordano, L.; Karayaylali, P.; Yu, Y.; Katayama, Y.; Maglia, F.; Lux, S.; Shao-Horn, Y. Chemical Reactivity Descriptor for the Oxide-Electrolyte Interface in Li-Ion Batteries. *J. Phys. Chem. Lett.* **2017**, *8*, 3881−3887.

(3) Yu, Y.; Karayaylali, P.; Katayama, Y.; Giordano, L.; Gauthier, M.; Maglia, F.; Jung, R.; Lund, I.; Shao-Horn, Y. Coupled $LiPF_6$ Decomposition and Carbonate Dehydrogenation Enhanced by Highly Covalent Metal Oxides in High-Energy Li-Ion Batteries. *J. Phys. Chem. C* **2018**, *122*, 27368−27382.

(4) Cherkashinin, G.; Motzko, M.; Schulz, N.; Späth, T.; Jaegermann, W. Electron Spectroscopy Study of Li[Ni,Co,Mn]O2/Electrolyte Interface: Electronic Structure, Interface Composition, and Device Implications. *Chem. Mater.* **2015**, *27*, 2875−2887.

(5) Li, W.; Asl, H. Y.; Xie, Q.; Manthiram, A. Collapse of $LiNi_{1-x-y}Co_xMnyO_2$ Lattice at Deep Charge Irrespective of Nickel Content in Lithium-Ion Batteries. *J. Am. Chem. Soc.* **2019**, *141*, 5097−5101.

(6) Kondrakov, A. O.; Schmidt, A.; Xu, J.; Geβwein, H.; Mönig, R.; Hartmann, P.; Sommer, H.; Brezesinski, T.; Janek, J. J. Anisotropic Lattice Strain and Mechanical Degradation of High- and Low-Nickel NCM Cathode Materials for Li-Ion Batteries. *J. Phys. Chem. C* **2017**, *121*, 3286−3294.

(7) Zhang, F.; Lou, S.; Li, S.; Yu, Z.; Liu, Q.; Dai, A.; Cao, C.; Toney, M. F.; Ge, M.; Xiao, X.; Lee, W.-K.; Yao, Y.; Deng, J.; Liu, T.; Tang, Y.; Yin, G.; Lu, J.; Su, D.; Wang, J. Surface Regulation Enables High Stability of Single-Crystal Lithium-Ion Cathodes at High Voltage. *Nat. Commun.* **2020**, *11*, 3050.

(8) Tian, C.; Xu, Y.; Tian, C.; Xu, Y.; Nordlund, D.; Lin, F.; Liu, J.; Sun, Z.; Liu, Y. Charge Heterogeneity and Surface Chemistry in Polycrystalline Cathode Materials. *Joule* **2018**, *2*, 464−477.

(9) Zhang, Y.; Yang, Z.; Tian, C. Probing and Quantifying Cathode Charge Heterogeneity in Li Ion Batteries. *J. Mater. Chem. A* **2019**, *7*, 23628−23661.

(10) Miller, D. J.; Proff, C.; Wen, J. G.; Abraham, D. P.; Bareño, J. Observation of Microstructural Evolution in Li Battery Cathode Oxide Particles by In Situ Electron Microscopy. *Adv. Energy Mater.* **2013**, *3*, 1098−1103.

(11) Liu, H.; Wolf, M.; Karki, K.; Yu, Y.-S.; Stach, E. A.; Cabana, J.; Chapman, K. W.; Chupas, P. J. Intergranular Cracking as a Major Cause of Long-Term Capacity Fading of Layered Cathodes. *Nano Lett.* **2017**, *17*, 3452−3457.

(12) Mao, Y.; Wang, X.; Xia, S.; Zhang, K.; Wei, C.; Bak, S.; Shadike, Z.; Liu, X.; Yang, Y.; Xu, R.; Pianetta, P.; Ermon, S.; Stavitski, E.; Zhao, K.; Xu, Z.; Lin, F.; Yang, X.; Hu, E.; Liu, Y. High-Voltage Charging-Induced Strain, Heterogeneity, and Micro-Cracks in Secondary Particles of a Nickel-Rich Layered Cathode Material. *Adv. Funct. Mater.* **2019**, *29*, 1900247.

(13) Su, Y.; Cui, S.; Zhuo, Z.; Yang, W.; Wang, X.; Pan, F. Enhancing the High-Voltage Cycling Performance of $LiNi_{0.5}Mn_{0.3}Co_{0.2}O_2$ by Retarding Its Interfacial Reaction with an Electrolyte by Atomic-Layer-Deposited Al_2O_3. *ACS Appl. Mater. Interfaces* **2015**, *7*, 25105−25112.

(14) Shi, Y.; Zhang, M.; Qian, D.; Meng, Y. S. Ultrathin Al_2O_3 Coatings for Improved Cycling Performance and Thermal Stability of $LiNi_{0.5}Co_{0.2}Mn_{0.3}O_2$ Cathode Material. *Electrochim. Acta* **2016**, *203*, 154−161.

(15) Mohanty, D.; Dahlberg, K.; King, D. M.; David, L. A.; Sefat, A. S.; Wood, D. L.; Daniel, C.; Dhar, S.; Mahajan, V.; Lee, M.; Albano, F. Modification of Ni-Rich FCG NMC and NCA Cathodes by Atomic

Layer Deposition: Preventing Surface Phase Transitions for High-Voltage Lithium-Ion Batteries. *Sci. Rep.* **2016**, *6*, 26532.
(16) Laskar, M. R.; Jackson, D. H. K.; Xu, S.; Hamers, R. J.; Morgan, D.; Kuech, T. F. Atomic Layer Deposited MgO: A Lower Overpotential Coating for $Li[Ni_{0.5}Mn_{0.3}Co_{0.2}]O_2$Cathode. *ACS Appl. Mater. Interfaces* **2017**, *9*, 11231−11239.
(17) Ahn, J.; Jang, E. K.; Yoon, S.; Lee, S. J.; Sung, S. J.; Kim, D. H.; Cho, K. Y. Ultrathin ZrO_2 on $LiNi_{0.5}Mn_{0.3}Co_{0.2}O_2$ Electrode Surface via Atomic Layer Deposition for High-Voltage Operation in Lithium-Ion Batteries. *Appl. Surf. Sci.* **2019**, *484*, 701−709.
(18) Gao, H.; Cai, J.; Xu, G. L.; Li, L.; Ren, Y.; Meng, X.; Amine, K.; Chen, Z. Surface Modification for Suppressing Interfacial Parasitic Reactions of a Nickel-Rich Lithium-Ion Cathode. *Chem. Mater.* **2019**, *31*, 2723−2730.
(19) Hu, W.; Zhang, C.; Jiang, H.; Zheng, M.; Wu, Q. H.; Dong, Q. Improving the Electrochemistry Performance of Layer $LiNi_{0.5}Mn_{0.3}Co_{0.2}O_2$ Material at 4.5 V Cutoff Potential Using Lithium Metaborate. *Electrochim. Acta* **2017**, *243*, 105−111.
(20) Wang, J.; Yu, Y.; Li, B.; Fu, T.; Xie, D.; Cai, J.; Zhao, J. Improving the Electrochemical Properties of $LiNi_{0.5}Co_{0.2}Mn_{0.3}O_2$ at 4.6 V Cutoff Potential by Surface Coating with Li_2TiO_3 for Lithium-Ion Batteries. *Phys. Chem. Chem. Phys.* **2015**, *17*, 32033−32043.
(21) Chen, Z.; Qin, Y.; Amine, K.; Sun, Y.-K. Role of Surface Coating on Cathode Materials for Lithium-Ion Batteries. *J. Mater. Chem.* **2010**, *20*, 7606−7612.
(22) Duan, J.; Tang, X.; Dai, H.; Yang, Y.; Wu, W.; Wei, X.; Huang, Y. Building Safe Lithium-Ion Batteries for Electric Vehicles: A Review. *Electrochem. Energy Rev.* **2020**, *3*, 1−42.
(23) Li, Y.; Yan, K.; Lee, H.-W. W.; Lu, Z.; Liu, N.; Cui, Y. Growth of Conformal Graphene Cages on Micrometre-Sized Silicon Particles as Stable Battery Anodes. *Nat. Energy* **2016**, *1*, 15029.
(24) Park, K.-Y.; Lim, J.-M.; Luu, N. S.; Downing, J. R.; Wallace, S. G.; Chaney, L. E.; Yoo, H.; Hyun, W. J.; Kim, H.-U.; Hersam, M. C. Concurrently Approaching Volumetric and Specific Capacity Limits of Lithium Battery Cathodes via Conformal Pickering Emulsion Graphene Coatings. *Adv. Energy Mater.* **2020**, *10*, 2001216.
(25) Lim, J.-M.; Luu, N. S.; Park, K.-Y.; Tan, M. T. Z.; Kim, S.; Downing, J. R.; He, K.; Dravid, V. P.; Hersam, M. C. Enhancing Nanostructured Nickel-Rich Lithium-Ion Battery Cathodes via Surface Stabilization. *J. Vac. Sci. Technol., A* **2020**, *38*, No. 063210.
(26) Shim, J. H.; Kim, Y. M.; Park, M.; Kim, J.; Lee, S. Reduced Graphene Oxide-Wrapped Nickel-Rich Cathode Materials for Lithium Ion Batteries. *ACS Appl. Mater. Interfaces* **2017**, *9*, 18720−18729.
(27) Lim, J.-M.; Kim, S.; Luu, N. S.; Downing, J. R.; Tan, M. T. Z.; Park, K.-Y.; Hechter, J. C.; Dravid, V. P.; He, K.; Hersam, M. C. High Volumetric Energy and Power Density Li_2TiSiO_5 Battery Anodes via Graphene Functionalization. *Matter* **2020**, *3*, 522−533.
(28) Chen, K. S.; Xu, R.; Luu, N. S.; Secor, E. B.; Hamamoto, K.; Li, Q.; Kim, S.; Sangwan, V. K.; Balla, I.; Guiney, L. M.; Seo, J. W. T.; Yu, X.; Liu, W.; Wu, J.; Wolverton, C.; Dravid, V. P.; Barnett, S. A.; Lu, J.; Amine, K.; Hersam, M. C. Comprehensive Enhancement of Nanostructured Lithium-Ion Battery Cathode Materials via Conformal Graphene Dispersion. *Nano Lett.* **2017**, *17*, 2539−2546.
(29) Secor, E. B.; Prabhumirashi, P. L.; Puntambekar, K.; Geier, M. L.; Hersam, M. C. Inkjet Printing of High Conductivity, Flexible Graphene Patterns. *J. Phys. Chem. Lett.* **2013**, *4*, 1347−1351.
(30) De Moraes, A. C. M.; Obrzut, J.; Sangwan, V. K.; Downing, J. R.; Chaney, L. E.; Patel, D. K.; Elmquist, R. E.; Hersam, M. C. Elucidating Charge Transport Mechanisms in Cellulose-Stabilized Graphene Inks. *J. Mater. Chem. C* **2020**, *8*, 15086−15091.
(31) Lin, F.; Markus, I. M.; Nordlund, D.; Weng, T.-C.; Asta, M. D.; Xin, H. L.; Doeff, M. M. Surface Reconstruction and Chemical Evolution of Stoichiometric Layered Cathode Materials for Lithium-Ion Batteries. *Nat. Commun.* **2014**, *5*, 3529.
(32) Li, G.; You, L.; Wen, Y.; Zhang, C.; Huang, B.; Chu, B.; Wu, J.-H.; Huang, T.; Yu, A. Ultrathin Li−Si−O Coating Layer to Stabilize the Surface Structure and Prolong the Cycling Life of Single-Crystal $LiNi_{0.6}Co_{0.2}Mn_{0.2}O_2$ Cathode Materials at 4.5 V. *ACS Appl. Mater. Interfaces* **2021**, *13*, 10952−10963.
(33) Radin, M. D.; Alvarado, J.; Meng, Y. S.; Van Der Ven, A. Role of Crystal Symmetry in the Reversibility of Stacking-Sequence Changes in Layered Intercalation Electrodes. *Nano Lett.* **2017**, *17*, 7789−7795.
(34) Shafiei Sabet, P.; Sauer, D. U. Separation of Predominant Processes in Electrochemical Impedance Spectra of Lithium-Ion Batteries with Nickel-Manganese-Cobalt Cathodes. *J. Power Sources* **2019**, *425*, 121−129.
(35) Sánchez-González, J.; Macías-García, A.; Alexandre-Franco, M. F.; Gómez-Serrano, V. Electrical Conductivity of Carbon Blacks under Compression. *Carbon* **2005**, *43*, 741−747.
(36) Yin, S.-C.; Rho, Y.-H.; Swainson, I.; Nazar, L. F. X-Ray/Neutron Diffraction and Electrochemical Studies of Lithium De/Re-Intercalation in $Li_{1-X}Co_{1/3}Ni_{1/3}Mn_{1/3}O_2$ ($x = 0 \rightarrow 1$). *Chem. Mater.* **2006**, *18*, 1901−1910.
(37) Lim, J.-M.; Hwang, T.; Kim, D.; Park, M.; Cho, K.; Cho, M. Intrinsic Origins of Crack Generation in Ni-Rich $LiNi_{0.8}Co_{0.1}Mn_{0.1}O_2$ Layered Oxide Cathode Material. *Sci. Rep.* **2017**, *7*, 39669.
(38) Strzemiecka, B.; Voelkel, A.; Donate-Robles, J.; Martín-Martínez, J. M. Assessment of the Surface Chemistry of Carbon Blacks by TGA-MS, XPS and Inverse Gas Chromatography Using Statistical Chemometric Analysis. *Appl. Surf. Sci.* **2014**, *316*, 315−323.
(39) Secor, E. B.; Lim, S.; Zhang, H.; Frisbie, C. D.; Francis, L. F.; Hersam, M. C. Gravure Printing of Graphene for Large-Area Flexible Electronics. *Adv. Mater.* **2014**, *26*, 4533−4538.
(40) Secor, E. B.; Gao, T. Z.; Islam, A. E.; Rao, R.; Wallace, S. G.; Zhu, J.; Putz, K. W.; Maruyama, B.; Hersam, M. C. Enhanced Conductivity, Adhesion, and Environmental Stability of Printed Graphene Inks with Nitrocellulose. *Chem. Mater.* **2017**, *29*, 2332−2340.
(41) Li, W.; Dolocan, A.; Oh, P.; Celio, H.; Park, S.; Cho, J.; Manthiram, A. Dynamic Behaviour of Interphases and Its Implication on High-Energy-Density Cathode Materials in Lithium-Ion Batteries. *Nat. Commun.* **2017**, *8*, 14589.
(42) Yang, X.; Chen, J.; Zheng, Q.; Tu, W.; Xing, L.; Liao, Y.; Xu, M.; Huang, Q.; Cao, G.; Li, W. Mechanism of Cycling Degradation and Strategy to Stabilize a Nickel-Rich Cathode. *J. Mater. Chem. A* **2018**, *6*, 16149−16163.
(43) Jiang, Y.; Qin, C.; Yan, P.; Sui, M. Origins of Capacity and Voltage Fading of $LiCoO_2$ upon High Voltage Cycling. *J. Mater. Chem. A* **2019**, *7*, 20824−20831.
(44) Chen, Z.; Dahn, J. R. Methods to Obtain Excellent Capacity Retention in $LiCoO_2$ Cycled to 4. 5 V. *Electrochim. Acta* **2004**, *49*, 1079−1090.
(45) Yano, A.; Shikano, M.; Ueda, A.; Sakaebe, H.; Ogumi, Z. $LiCoO_2$ Degradation Behavior in the High-Voltage Phase Transition Region and Improved Reversibility with Surface Coating. *J. Electrochem. Soc.* **2017**, *164*, A6116−A6122.
(46) Seong, W. M.; Yoon, K.; Lee, M. H.; Jung, S. K.; Kang, K. Unveiling the Intrinsic Cycle Reversibility of a $LiCoO_2$ Electrode at 4. 8-V Cutoff Voltage through Subtractive Surface Modification for Lithium-Ion Batteries. *Nano Lett.* **2019**, *19*, 29−37.
(47) Li, H.; Zhang, N.; Li, J.; Dahn, J. R. Updating the Structure and Electrochemistry of Li_xNiO_2 for $0 \leq x \leq 1$. *J. Electrochem. Soc.* **2018**, *165*, A2985−A2993.
(48) Li, W.; Reimers, J. N.; Dahn, J. R. In Situ X-Ray Diffraction and Electrochemical Studies of Li1-$XNiO_2$. *Solid State Ionics* **1993**, *67*, 123−130.
(49) Croguennec, L.; Pouillerie, C.; Mansour, A. N.; Delmas, C. Structural Characterisation of the Highly Deintercalated $LixNi_{1.02}O_2$ Phases (with $X \leq 0.30$). *J. Mater. Chem.* **2001**, *11*, 131−141.
(50) Choi, J.; Manthiram, A. Role of Chemical and Structural Stabilities on the Electrochemical Properties of Layered $LiNi_{1/3}Mn_{1/3}Co_{1/3}O_2$ Cathodes. *J. Electrochem. Soc.* **2005**, *152*, A1714.
(51) Gent, W. E.; Li, Y.; Ahn, S.; Lim, J.; Liu, Y.; Wise, A. M.; Gopal, C. B.; Mueller, D. N.; Davis, R.; Weker, J. N.; Park, J.-H.; Doo, S.-K.; Chueh, W. C. Persistent State-of-Charge Heterogeneity in Relaxed,

Partially Charged $Li_{1-x}Ni_{1/3}Co_{1/3}Mn_{1/3}O_2$ Secondary Particles. *Adv. Mater.* **2016**, *28*, 6631−6638.
(52) Li, S.; Jiang, Z.; Han, J.; Xu, Z.; Wang, C.; Huang, H.; Yu, C.; Lee, S.-J.; Pianetta, P.; Ohldag, H.; Qiu, J.; Lee, J.-S.; Lin, F.; Zhao, K.; Liu, Y. Mutual Modulation between Surface Chemistry and Bulk Microstructure within Secondary Particles of Nickel-Rich Layered Oxides. *Nat. Commun.* **2020**, *11*, 4433.
(53) Yang, Y.; Xu, R.; Zhang, K.; Lee, S.; Mu, L.; Liu, P.; Waters, C. K.; Spence, S.; Xu, Z.; Wei, C.; Kautz, D. J.; Yuan, Q.; Dong, Y.; Yu, Y.-S.; Xiao, X.; Lee, H.-K.; Pianetta, P.; Cloetens, P.; Lee, J.-S.; Zhao, K.; Lin, F.; Liu, Y. Quantification of Heterogeneous Degradation in Li-Ion Batteries. *Adv. Energy Mater.* **2019**, *9*, 1900674.
(54) Jiang, Z.; Li, J.; Yang, Y.; Mu, L.; Wei, C.; Yu, X.; Pianetta, P.; Zhao, K.; Cloetens, P.; Lin, F.; Liu, Y. Machine-Learning-Revealed Statistics of the Particle-Carbon/Binder Detachment in Lithium-Ion Battery Cathodes. *Nat. Commun.* **2020**, *11*, 2310.
(55) Mukhopadhyay, A.; Sheldon, B. W. Deformation and Stress in Electrode Materials for Li-Ion Batteries. *Prog. Mater. Sci.* **2014**, *63*, 58−116.
(56) Min, K.; Cho, E. Intrinsic Origin of Intra-Granular Cracking in Ni-Rich Layered Oxide Cathode Materials. *Phys. Chem. Chem. Phys.* **2018**, *20*, 9045−9052.
(57) Molenda, J.; Wilk, P.; Marzec, J. Structural, Electrical and Electrochemical Properties of $LiNiO_2$. *Solid State Ionics* **2002**, *146*, 73−79.
(58) Amin, R.; Chiang, Y.-M. Characterization of Electronic and Ionic Transport in $Li_{1-X}Ni_{0.33}Mn_{0.33}Co_{0.33}O_2$(NMC333) and $Li_{1-X}Ni_{0.5}0Mn_{0.20}Co_{0.30}O_2$(NMC523) as a Function of Li Content. *J. Electrochem. Soc.* **2016**, *163*, A1512−A1517.
(59) Wan, T. H.; Saccoccio, M.; Chen, C.; Ciucci, F. Influence of the Discretization Methods on the Distribution of Relaxation Times Deconvolution: Implementing Radial Basis Functions with DRTtools. *Electrochim. Acta* **2015**, *184*, 483−499.
(60) Toby, B. H.; Von Dreele, R. B. GSAS-II: The Genesis of a Modern Open-Source All Purpose Crystallography Software Package. *J. Appl. Crystallogr.* **2013**, *46*, 544−549.

https://doi.org/10.1021/acsaem.1c01995
ACS Appl. Energy Mater. 2021, 4, 11069−11079